

# Two-dimensional electron systems in perovskite oxide heterostructures: Role of the polarity-induced substitutional defects

Shih-Chieh Lin,<sup>1,2</sup> Cheng-Tai Kuo,<sup>1,2,3,\*</sup> Yu-Cheng Shao,<sup>4</sup> Yi-De Chuang,<sup>4</sup> Jaap Geessinck,<sup>5</sup> Mark Huijben,<sup>5</sup> Jean-Pascal Rueff,<sup>6,7</sup> Ismael L. Graff,<sup>8</sup> Giuseppina Conti,<sup>1,2</sup> Yingying Peng,<sup>9,#</sup> Aaron Bostwick,<sup>4</sup> Eli Rotenberg,<sup>4</sup> Eric Gullikson,<sup>2</sup> Slavomír Nemsák,<sup>4</sup> Arturas Vailionis,<sup>10,11</sup> Nicolas Gauquelin,<sup>5,12</sup> Johan Verbeeck,<sup>12</sup> Giacomo Ghiringhelli,<sup>9</sup> Claus M. Schneider,<sup>1,13</sup> and Charles S. Fadley<sup>1,2,†</sup>

<sup>1</sup>*Department of Physics, University of California Davis, Davis, California 95616, USA*

<sup>2</sup>*Materials Sciences Division, Lawrence Berkeley National Laboratory, Berkeley, California 94720, USA*

<sup>3</sup>*Stanford Synchrotron Radiation Lightsource, SLAC National Accelerator Laboratory, Menlo Park, California 94025, USA*

<sup>4</sup>*Advanced Light Source, Lawrence Berkeley National Laboratory, Berkeley, California 94720, USA*

<sup>5</sup>*Faculty of Science and Technology and MESA+ Institute for Nanotechnology, University of Twente, Enschede 7500 AE, The Netherlands*

<sup>6</sup>*Synchrotron SOLEIL, L'Orme des Merisiers, Saint-Aubin-BP48, 91192 Gif-sur-Yvette, France*

<sup>7</sup>*Sorbonne Université, CNRS, Laboratoire de Chimie Physique-Matière et Rayonnement, 75005 Paris, France*

<sup>8</sup>*Department of Physics, Federal University of Paraná, Curitiba, Brazil*

<sup>9</sup>*CNR-SPIN and Dipartimento di Fisica Politecnico di Milano, Piazza Leonardo da Vinci 32, Milano I-20133, Italy*

<sup>10</sup>*Stanford Nano Shared Facilities, Stanford University, Stanford, California 94305, USA*

<sup>11</sup>*Department of Physics, Kaunas University of Technology, Studentu street 50, LT-51368 Kaunas, Lithuania*

<sup>12</sup>*Electron Microscopy for Materials Science (EMAT), University of Antwerp, Groenenborgerlaan 171, B-2020 Antwerp, Belgium*

<sup>13</sup>*Peter-Grünberg-Institut PGI-6, Forschungszentrum Jülich, Jülich 52425, Germany*

\* Email: ctkuo@slac.stanford.edu

# Present address: International Center for Quantum Materials, School of Physics, Peking University, Beijing 100871, China

† Deceased August 1, 2019.

## ABSTRACT

The discovery of a two-dimensional electron system (2DES) at the interfaces of perovskite oxides such as  $\text{LaAlO}_3$  and  $\text{SrTiO}_3$  has motivated enormous efforts in engineering interfacial functionalities with this type of oxide heterostructures. However, its fundamental origins are still not understood, e.g. the microscopic mechanisms of coexisting interface conductivity and magnetism. Here we report a comprehensive spectroscopic investigation of the depth profile of 2DES-relevant  $\text{Ti}^{3+}$  ions using depth- and element-specific techniques, standing-wave excited photoemission and resonant inelastic scattering. We found that  $\text{Ti}^{3+}$  ions which give rise to the 2DES are located within 3 unit cells from the n-type interface in the  $\text{SrTiO}_3$  layer. Unexpectedly, another type of  $\text{Ti}^{3+}$  ions, which are polarity-induced Ti-on-Al antisite defects, reside in the first 3 unit cells of the opposing

LaAlO<sub>3</sub> layer (~10 Å). Our findings suggest that the 2DES and 2D magnetism at the LaAlO<sub>3</sub>/SrTiO<sub>3</sub> interface have disparate explanations as originating from different types of Ti<sup>3+</sup> ions.

## Main

The discovery of conductivity at the polar-nonpolar interfaces of insulating oxides such as LaAlO<sub>3</sub> (LAO) and SrTiO<sub>3</sub> (STO) has revealed great potentials for engineering emergent interfacial functionalities absent in their bulk forms<sup>1,2,3,4,5</sup>. The two band insulators LAO and STO have the perovskite structure consisting of a mutual stacking of (LaO)<sup>+</sup> and (AlO<sub>2</sub>)<sup>-</sup>, and (SrO)<sup>0</sup> and (TiO<sub>2</sub>)<sup>0</sup> atomic layers, respectively, with their nominal valence values indicated. In the [001] direction, two different interfaces can be formed between the polar LAO and nonpolar STO: (LaO)<sup>+</sup>/(TiO<sub>2</sub>)<sup>0</sup> (named n-type) and (SrO)<sup>0</sup>/(AlO<sub>2</sub>)<sup>-</sup> (named p-type)<sup>1,2,3</sup>. A remarkable feature is that the two-dimensional electron system (2DES) can only form at the n-type interface when the thickness of the top LAO is over the critical thickness of 3 unit cells (uc)<sup>3</sup>.

How is this 2DES established in the first place? While there is some consensus that its origin may be associated with the Ti 3d electrons at the interfaces<sup>6</sup>, the underlying microscopic mechanisms are far from being understood. A variety of suggestions have been put forward to some of the experimental observations, but they usually address only specific aspects and are yet unable to provide a consistent solution to all the puzzles, such as the existence of critical thickness, interface conductivity, interface magnetism, etc.<sup>1,2,3,7,8,9,10,11,12,13,14,15,16</sup>. In 2014 Yu and Zunger took a very interesting approach and went beyond the view of a mere electronic reconstruction. On the basis of first principles calculations, they proposed the so-called polarity-induced defect mechanism<sup>17</sup>. It predicts

that defects spontaneously form at the LAO surface and/or LAO/STO interfaces in order to compensate the polar-discontinuity-induced built-in field, and in this way avoid a divergence to the electric potential. Consequently, the formation of 2DES and the appearance of interface magnetism ought to be driven by polar-field-induced defects, such as the paired antisite and oxygen vacancy defects<sup>17</sup>. Exploring such defects in experiments is a challenging task and asks for sophisticated approaches, which are able to extract information specifically from the interface.

X-ray photoemission spectroscopy is a powerful tool for revealing the interface electronic structure and has provided valuable information regarding the electronic reconstruction and quantum confinement effect of these occupied Ti 3*d* states that contribute to 2DES<sup>18, 19, 20, 21, 22, 23</sup>. More specifically, resonant X-ray photoemission spectroscopy (RXPS) can enhance the spectral weight of Ti<sup>3+</sup> states and thus has been widely used to study the interface electronic structure of LAO/STO heterostructures<sup>20, 21, 22, 23</sup>. A quite complementary information about the Ti electronic states can be obtained from resonant inelastic X-ray scattering (RIXS). It probes Ti 3*d* orbital transitions, namely *dd* excitations, between occupied and unoccupied states<sup>24, 25, 26</sup>. As a drawback, neither conventional photoemission nor RIXS are able to probe the depth profile of the emitted photoelectrons or scattering photons across an interface. Such a profile is strongly needed, however, to evaluate the real space distribution of the Ti<sup>3+</sup> ions in the LAO/STO interface. By contrast, cross-sectional scanning probe microscopies (XSPM) and scanning transmission electron microscopy (STEM) offer high spatial resolution and have been widely used to study the local electronic properties relative to the 2DES of LAO/STO heterostructures<sup>7, 27, 28, 29, 30</sup>, but they cannot resolve the electronic/orbital states.

Some advanced STEM studies were able to localize electronic states and hybridization<sup>31</sup> and image orbitals<sup>32</sup> but they are limited in the determination of orbital character due to low q-resolution<sup>31</sup> and subject to instrumental effects and delocalization of the inelastic scattering<sup>33,34</sup>.

We have demonstrated in prior works that standing wave-excited (SW) spectroscopic techniques, such as SW-RXPS, SW hard X-ray photoemission spectroscopy (SW-HXPS)<sup>35,36,37,38,39</sup>, and SW-RIXS<sup>40</sup>, are capable of disentangling the physics at buried interfaces in terms of depth profiling the elemental diffusions, polarisation-induced voltage drop, and orbital and magnetic excitations. They are thus uniquely suited to elucidate the formation of the 2DES at the LAO/STO interface. In this work, we have therefore used a full suite of SW-excited spectroscopic approaches to extract the depth profile of the orbital character of  $\text{Ti}^{3+}$  ions across the LAO/STO interfaces and to detail its influence on the interface conductivity and magnetism.

**Depth sensitivity of X-ray standing wave techniques.** Figure 1a shows a schematic of SW measurements for this specific sample configuration. The superlattice sample consists of 20 bilayers of 5 uc LAO and 5 uc STO layers on a  $\text{TiO}_2$ -terminated STO (001) substrate. The LAO layer in each bilayer is slightly thicker than the critical thickness, which is the best choice for visualising how these defects and 2DES distribute across the LAO/STO interfaces. To better demonstrate the difference in the depth sensitivity for these SW techniques, their calculated yield strength distributions are shown in Fig. 1b-d. Figure 1b and c are the SW-HXPS ( $h\nu = 3000$  eV) and SW-RXPS ( $h\nu = 459$  eV) photoemission yield distributions, respectively, while Fig. 1d is the SW-RIXS ( $h\nu = 459.3$  eV) yield

distribution. The probing depth for RXPS, HXPS, and RIXS determined from the yield distributions is  $\sim 27$ , 135, and 960 Å, respectively (see Methods), and the shorter depth for RXPS and HXPS relative to RIXS is due to the shorter escape depth for photoelectrons. Hence, SW-RXPS is sensitive to the top LAO layer and the first interface, SW-HXPS is sensitive to the top 3 LAO/STO (STO/LAO) interfaces, and SW-RIXS is sensitive to all 20 LAO/STO (STO/LAO) interfaces. We have combined these different depth sensitivities to obtain a more consistent picture.

Although RIXS has the longest probing depth among these SW techniques, its signal comes only from the Ti ions in the STO layer, a partial information that cannot be used to derive the full sample structure as done with SW photoemission. Such short-fall can be circumvented by using the core-level rocking curves (RCs) from both SW-HXPS and SW-RXPS to better determine the multilayer structure. We note that the information obtained from HXPS is particularly useful for determining the depth profile of the quasi-particle (QP) peak measured with SW-RXPS and also the *dd* excitations from SW-RIXS.

**Standing-wave excited photoemission results.** Figure 2a&b show the experimental core-level spectra and their corresponding RCs (open circles) from representative La and Sr core-levels at  $h\nu = 3000$  eV and at  $h\nu = 459$  eV, respectively. The best-fit simulated core-level RCs (curves) are plotted together with the experimental RCs. The best-fit superlattice sample structure was determined by minimising the total difference between 8 experimental (both soft and hard X-rays) RCs and the simulated RCs simultaneously via iteratively adjusting the input structure. The whole fitting results regarding the core-level spectra and their RCs are shown in supplementary Fig. 3&4&5. The determination of best-

fit RCs is described in the Methods section. The best-fit results indicate that superlattice sample has reasonably sharp interface. The averaged interdiffusion between the interfaces is 7 Å with respect to the ideal sample and is in excellent agreement with the STEM results of 1~3 uc elemental diffusions (see supplementary Fig. 2)

Next, we focus on determining the depth profile of the  $\text{Ti}^{3+}$  electronic states using SW-RXPS. Using RXPS with excitation energies near the Ti  $L_3$  edge, the spectral weight of  $\text{Ti}^{3+}$  states in the valence band spectrum of LAO/STO heterostructures can be enhanced<sup>20,21,22,23</sup>. Figure 2c shows the RXPS valence band spectrum with an inset for a magnified view around the Fermi level where a quasiparticle (QP) peak centered at ~0.35 eV is observed. The slightly higher QP peak position with respect to the prior work<sup>20</sup> can be related to the limited energy resolution or from a different level of the impurities in different samples. The experimental QP (open circles) and its best-fit (curve) RCs are shown in Fig. 2b. The contrasting QP RC relative to other core-level RCs indicates that this QP component has its own depth distribution. Since QP comes from the Ti 3d orbitals, its depth distribution can be related to that of  $\text{Ti}^{3+}$  ions, or equivalently the 2DES in the STO layer<sup>20,22</sup>. From the depth profile at the first LAO/STO interface (see Fig. 2d), our SW-RXPS results suggest an unexpected source of  $\text{Ti}^{3+}$  with high concentration is observed in the LAO layer, which will be discussed later.

**Standing-wave excited resonant inelastic X-ray scattering results.** To gain further insight on the depth distribution of  $\text{Ti}^{3+}$  3d orbitals and its relationship to the 2DES formation, we have performed SW-RIXS measurements on the very same sample and the results are summarized in Figure 3. In order to distinguish the Raman-like excitations from

the normal fluorescence emission, the excitation-energy-dependent RIXS measurements were performed near the Ti L<sub>3</sub> edge, see Fig. 3a (the wider range energy loss spectrum showing the charge-transfer component can be found in supplementary Fig. 7). The *dd* component shows a constant Raman shift of ~2.6 eV, whereas the fluorescence has a linear shift with excitation photon energy. The chosen excitation energy for the SW-RIXS measurements was 1 eV below the e<sub>g</sub> resonance to better assist probing the Ti<sup>3+</sup> ions and separating the *dd* and fluorescence features. Based on the previous work, we can fit the SW-RIXS spectra with five peaks: quasi-elastic line,  $d_{xz}/d_{yz}$  (0.8 eV),  $d_{x^2-y^2}$  (2.7 eV),  $d_{z^2}$  excitations (3.2 eV), and fluorescence (~1.8 eV), as demonstrated in Fig. 3b<sup>24,25</sup>.

Their respective experimental RCs (open circles) and their best-fit results (curves) are shown in Figure 3c. To first order, we can anticipate that the *dd* excitations are coming from Ti<sup>3+</sup> ions with associated structural defects and the fluorescence is from the true 2DES phase. The intensity modulation around the Bragg angle (~20°) for these RCs are evidently different and they also do not fit to the simulated RC from the whole STO layer. Consequently, RIXS excitations must have different spatial distributions. Figure 3d shows the determined depth distributions in the top 2.5 LAO/STO bilayers for the RIXS excitations. The depth profile for each excitation in Fig. 3c was normalized in a way that its integrated intensity is proportional to the angular-averaged RIXS intensity of the corresponding excitations; therefore, the intensity of the depth profile represents a sort of “concentration” map of excitations in depth.

The SW-RIXS results show that there is a notably large amount of Ti<sup>3+</sup> residing in both the LAO and STO sides of the interface, which is consistent with the SW-RXPS results. These Ti<sup>3+</sup> reside at the n-type interfaces (LAO<sub>bottom</sub>/STO<sub>top</sub>) and show no

contributions at the p-type interfaces (STO\_bottom/LAO\_top), agreeing with experimental observations of interface conductivity<sup>1</sup>. In general, a RC with higher (lower) intensity modulation means a more localized (delocalized) distribution in the depth. The intensity modulations in Fig. 3c imply that the fluorescence originate from a wider distribution in depth, while the  $d_{x^2-y^2}$  excitations originate from narrower distributions. The possible cause of the variations of depth distributions in  $dd$  excitations will be discussed later.

The determined depth profile of the QP peak from SW-RXPS and  $dd$  excitations from SW-RIXS represent the depth profiles of  $\text{Ti}^{3+}$  ions. These results show that, in contrast to the general assumption that these  $\text{Ti}^{3+}$  are attributed to the mobile 2DES in the STO layer, there are two different sources residing in both LAO and STO. What does this phenomenon stand for? What is the relationship between these  $\text{Ti}^{3+}$  and 2DES?

In Figure 4, we illustrate the polarity-induced defect mechanism for the 2DES formation<sup>17</sup>. The polarity discontinuity across the LAO/STO interfaces triggers the spontaneous formation of multiple kinds of defects. In addition to the surface oxygen vacancy defects ( $\text{V}_{\text{O}(\text{S})}$ ), a kind of paired antisite defects like Ti-on-Al ( $\text{Ti}_{\text{Al}}$ ) and Al-on-Ti ( $\text{Al}_{\text{Ti}}$ ) from the hopping of Ti atoms near the interface into the  $\text{AlO}_2$  atomic layers and exchanging site with Al atoms, can be present in order to alleviate the polarisation-induced field across the interfaces. At this n-type interface, when the LAO thickness is below the critical thickness, all electrons are transferred from  $\text{Ti}_{\text{Al}}$  to  $\text{Al}_{\text{Ti}}$  defects with lowest formation energy to cancel the polar field and subsequently these electrons will be trapped by deep  $\text{Al}_{\text{Ti}}$  defects in the STO layer; as a consequence, these electrons become immobile. On the other hand, when the LAO thickness is above the critical thickness, the  $\text{V}_{\text{O}(\text{S})}$  defects are responsible for the cancelation of the built-in polar field<sup>17</sup>. Among the electrons ionized



from the  $V_{O(S)}$  defects, half of them are donated to the  $Al_{Ti}$  defects, and the rest form the 2DES in the STO layer. Meanwhile, the interface  $Ti_{Al}$  defects in the LAO layer ( $Ti^{3+}$  ions on  $Al^{3+}$  sites) donate no electrons. Some of the surface  $Ti_{Al}$  defects still tend to donate electrons and some remain ionized when the LAO thickness is larger than the critical thickness, but it will gradually be dominated by the  $V_{O(S)}$  defects with the increased LAO thickness. These  $Ti^{3+}$  ions in LAO can be probed by RXPS and RIXS.

The Ti ions in the STO layer can be regarded as the mobile 2DES, residing within the 3 uc STO layer ( $\sim 12 \text{ \AA}$  in length) near the interface, of which length scale is fairly consistent with the recent STEM results of  $\sim 10 \pm 03 \text{ \AA}$ <sup>30</sup>. The other Ti ions located at LAO layer can be the  $Ti_{Al}$  defects, residing within  $\sim 10 \text{ \AA}$  LAO layer near the interface. This length scale also perfectly matches to the critical thickness of 3 uc predicted by the first principles calculations<sup>17</sup>. Note that a little concentration of  $Ti_{Al}$  defects was also found at the LAO surface because some of the  $Ti_{Al}$  defects are ionized as  $Ti^{3+}$  at the LAO surface; this is also consistent to the polarity-induced defect mechanism<sup>17</sup>. These findings show strong experimental evidence that substantiates the polarity-induced defect mechanism.

The depth profiles of the QP and  $dd$  excitations all show the existence of the polarity-induced defects ( $Ti_{Al}$ ). Additionally, the  $Ti_{Al}$  defects and 2DES have identical QP peak and energy levels, meaning that they both exhibit orbital reconstructions and quantum confinement effects. This phenomenon implies a strong correlation between these  $Ti_{Al}$  defects and mobile 2DES. It is noteworthy that, according to the polarity-induced defect mechanism<sup>17</sup>, these trapped  $Ti^{3+}$  ions ( $Ti_{Al}$ ) in LAO layer are responsible for the interface magnetism, while the mobile 2DES in STO layer is responsible for the interface conductivity. The understanding of the interplay of the layers of mobile electrons and

trapped ions will be important to enable controlling both interface conductivity and magnetism, which should be investigated in the future.

For the results of SW-RIXS, the variations of depth distributions in  $dd$  excitations of Figure 3c might be seen as insignificant, without changing the main messages explained above. To give a meaning to the differences in the RC of the various  $dd$  contributions, the subband picture<sup>19,23,24</sup> sketched in Fig. 4b can be utilized. Due to the quantum confinement effect, the half-filled  $d_{xy}$  orbital is confined at the bottom of a quantum well and has the narrowest depth extension. In contrast, the  $d_{xz}/d_{yz}$  orbitals at higher energy are more weakly confined, and this effect is even stronger for the  $d_{x^2-y^2}$  and  $d_{z^2}$ . Finally, the fluorescence signal shows wider distribution with more contributions in STO layer. Indeed, the differences among the  $dd$  excitations depth profiles is an intriguing phenomenon, yet difficult to explain at qualitative level; a more quantitative interpretation will have to include the RIXS cross section and the quantum confinement and goes beyond the scope of present work.

We have demonstrated the coexistence of polarity-induced defects and 2DES across the polar/non-polar oxide interfaces, implying that the spontaneously formed defects for canceling the interfacial polarisation field are the fundamental origins of 2DES formation. Our findings indicate that the well-known assumption of  $\text{Ti}^{3+}$  ions, which is direct indication of 2DES formation, only existing in the STO side in the photoemission and RIXS studies is an oversimplified picture and should be revisited carefully. In addition, the interface conductivity and magnetism at LAO/STO could originate from different  $\text{Ti}^{3+}$  ions located in the STO and LAO layer, respectively. In a methodological perspective, we have demonstrated the power of combining SW photoemission and RIXS spectroscopies to

obtain the depth distribution of electronic/orbital states at buried interfaces with precision of a few Angstroms.

## Methods

**Sample synthesis.** The superlattice sample,  $[(\text{LaAlO}_3)_n/(\text{SrTiO}_3)_m]_p$ ,  $(\text{LAO}_n/\text{STO}_m)_p$  ( $n=5$  unit cell (uc),  $m=5$  uc, and  $p=20$ ), was deposited by pulsed laser deposition on a  $\text{TiO}_2$ -terminated Nb-doped  $\text{SrTiO}_3$  (001) substrate. The individual materials were ablated from single-crystalline  $\text{LaAlO}_3$  and  $\text{SrTiO}_3$  targets using a KrF excimer laser operating at 248 nm, while laser fluence and repetition rate were  $1.3 \text{ J/cm}^2$  and 1 Hz, respectively. To enable the formation of 2DES interfaces in LAO/STO multilayers an oxygen pressure of  $2 \times 10^{-3}$  mbar was applied, while maintaining a temperature of  $800^\circ\text{C}$ <sup>2,3,13</sup>. Reflective high-energy electron diffraction indicated layer-by-layer growth during the full superlattice growth and was used to enable unit-cell-control of all individual layers.

**Sample characterisation.** X-ray diffraction (XRD) analysis confirmed the epitaxial growth of the superlattice as it is fully strained in plane to the STO cubic structure. The highly ordered growth of the superlattice is further demonstrated by the observation of clear Laue fringes between the diffraction peaks (see Supplementary Fig. 1a). Analysis of the XRD results showed the coherent growth with a reduced c-axis parameter of  $3.73 \text{ \AA}$  for each LAO layer as compared to  $3.90 \text{ \AA}$  for each STO layer, which is in good agreement with previous reports<sup>11,41,42</sup>. The low level of surface roughness was confirmed by atomic force microscopy analysis of the surface of the LAO/STO superlattice, indicating the presence of smooth terraces separated by clear, single-unit-cell height steps similar to the surface of the initial  $\text{TiO}_2$ -terminated STO (001) substrate (see Supplementary Fig. 1b).

The structural and chemical quality of the sample have been verified on the local scale by scanning transmission electron microscopy (STEM) high angle annular dark field (HAADF) imaging (Z-Contrast) and electron energy loss spectroscopy (EELS) (See Supplementary Fig. 2). STEM was performed on a Titan microscope operated at 300keV with a probe semi convergence angle of 21 mrad; EELS measurements were performed collecting the Ti L<sub>2,3</sub>, Sr L<sub>2,3</sub> edge, O K and La M<sub>4,5</sub> and Al K edges simultaneously. The acquisition parameters were 0.04 s/pixel, 0.2 Å/pixel and 0.5 eV/pixel for mapping in the dual EELS mode. Collection semi-angles for HAADF imaging and EELS were 41-94 mrad and 94 mrad, respectively. STEM results show the superlattice sample has sharp and well-controlled interfaces, demonstrating compatible observations to the prior works<sup>7,43</sup>.

**Standing wave excited hard and resonant X-ray photoemission (SW-HXPS and SW-RXPS) measurements.** SW-RXPS measurements were performed at the beamline MAESTRO of Advanced Light Source, Lawrence Berkeley National Laboratory. SW-HXPS measurements were performed at the beamline GALAXIES of SOLEIL synchrotron. The synchrotron radiation light was *p*-polarised. The energy resolution of SW-RXPS is 500 meV and that of SW-HXPS is 440 meV. Both measurements were performed at room temperature for preventing the charging effect. The details of GALAXIES endstation can be found elsewhere<sup>44</sup>.

**Standing wave excited resonant inelastic x-ray scattering (SW-RIXS) measurements.** SW-RIXS measurements were performed at the qRIXS endstation at beamline 8.0.1.3 at the Advanced Light Source, Lawrence Berkeley National Laboratory. The combined energy resolution of the SW-RIXS is 360 meV determined from the FWHM of the elastic peak. The multilayer sample was cooled down to ~78K by liquid N<sub>2</sub> during the

measurements. The RIXS measurements were probed by p-polarised x-ray with a scattering angle of 115 degree near the Ti L<sub>3</sub> edge. The details of qRIXS endstation can be found elsewhere<sup>45</sup>.

**X-ray optics calculations of SW effect in photoemission and RIXS.** The SW is generated by the interference between the incident and reflected waves, and it satisfies this equation  $\lambda = 2d_{BL}\sin \theta_B$ , where  $\lambda$  is the wavelength of the incident X-rays,  $d_{BL}$  is the thickness of the bilayer, and  $\theta_B$  is the Bragg angle. The resulting SW electric-field intensity varies sinusoidally with respect to the sample depth and has a periodicity very close to  $d_{BL}$ . Scanning the incidence angle over the Bragg peak moves the SW vertically by half of its wavelength, and this variation provides phase-sensitive depth resolution for photoemission and RIXS. The vertical movement of the SW through the sample with changing the incidence angle will thus enhance or reduce photoemission/RIXS signals from different depths, generating what are called rocking curves (RC).

An X-ray optics computing code (Yang X-ray Optics, YXRO<sup>37</sup>) has been used for generating yield intensity map and analysing the experimental RC data. The probing depth for SW photoemission is defined as  $3\lambda$ , where  $\lambda$  is the effective inelastic mean free paths. The probing depth for SW-RIXS is defined as  $3\Lambda$ , where  $\Lambda$  is the effective attenuation lengths. The yield intensities are SW intensities multiplied by an attenuation term which takes into account  $\lambda_{RXPS}/\lambda_{HXPS}$  for the photoelectron peaks or  $\Lambda$  for the RIXS excitations peaks. The optical constants used for the simulations with excitation energies near the Ti L<sub>3</sub> edge were calculated from a Ti XAS spectrum using Kramers-Kronig relations.

The core-level RCs measured by SW-HXPS and SW-RXPS represent the intensities of photoelectrons collected from the elements distributed uniformly in either the LAO or STO

layer. Their best-fit RCs are determined by minimizing the errors between the experimental and simulated RCs simultaneously via iteratively adjusting the input structure. (e.g. the LAO thickness). The QP RC for SW-RXPS and  $dd$  and fluorescence RCs for SW-RIXS don't have uniform distribution and thus have depth profiles with each point at a specific depth having a weighting coefficient. For these kinds of experimental RCs, their best-fit RCs are determined by minimising the errors between the experimental and simulated RCs simultaneously via optimising the weighting coefficients (BFGS method). As an example, we choose the QP RC to show the difference between the experimental and simulated RCs using the optimised (best-fit), step-like ( $d_{\text{delta}}=1\sim15 \text{ \AA}$ ), and uniform ( $d_{\text{delta}}= \text{whole STO layer}$ ), distributions. The optimised distributions show the best results in terms of minimizing the errors. More discussions on determining the depth profiles can be found elsewhere<sup>40</sup>.

## ACKNOWLEDGMENTS

We thank Gabriella Maria De Luca and Lucio Braicovich for discussions. Charles S. Fadley was deceased on August 1, 2019. We thank his significant contributions to this work. We thank Advanced Light Source for the access to Beamline 8.0.3 (qRIXS) via Proposal No. 09892 and beamline 7.0.2 (MAESTRO) via Proposal No. RA-00291 that contributed to the results presented here. We thank synchrotron SOLEIL (via Proposal No. 99180118) for the access to Beamline GALAXIES. This work was supported by the US Department of Energy under Contract No. DE-AC02-05CH11231 (Advanced Light Source), and by DOE Contract No. DE-SC0014697 through the University of California, Davis (S.-C.L., C.-T.K, and C.S.F.), and from the Jülich Research Center, Peter Grünberg

Institute, PGI-6. I. L. G. wishes to thank Brazilian scientific agencies CNPQ (Project No. 200789/2017-1) and CAPES (CAPES-PrInt-UFPR) for their financial support. J.V. and N.G. acknowledge funding from the Geconcentreerde Onderzoekacties (GOA) project “Solarpaint” of the University of Antwerp and the European Union’s horizon 2020 research and innovation program ESTEEM3 under grant agreement n°823717. The Qu-Ant-EM microscope used in this study was partly funded by the Hercules fund from the Flemish Government.

### **Author contributions**

S.-C.L. and C.-T.K. carried out the SW-RXPS measurements using the MAESTRO beamline with assistance from A.B. and E.R.. S.-C.L. and I.L.G. carried out the SW-HXPS measurements using the GALAXIES beamline with assistance from J.-P.R.. S.-C.L. and C.-T.K. carried out the SW-RIXS measurements using the qRIXS beamline with assistance from Y.-C.S. and Y.-D.C.. J.G. and M.H. grew the LAO/STO superlattice. J.G., M.H., and A.V. performed AFM and XRD characterisation. N.G. and J.V. performed and analysed the STEM measurement. S.-C.L. and C.-T.K. carried out the data analysis with feedbacks from G.C. and C.S.F.. Y.P. and G.G. provided advices regarding RIXS analysis. C.-T.K. and S.-C.L. wrote the manuscript with feedbacks from G.G.. All coauthors contributed to the manuscript. C.S.F. was the principal investigator of the project.

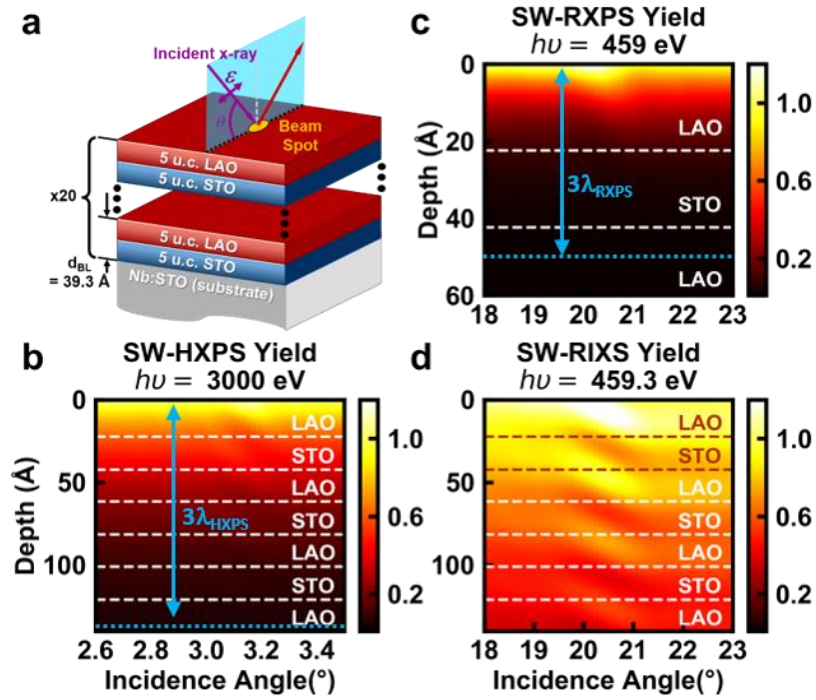


**Figure 1 | Depth sensitivity of SW techniques for the LAO/STO superlattice.** (a) The superlattice sample,  $(\text{LAO}_n/\text{STO}_m)_p$  ( $n = 5$  uc,  $m = 5$  uc, and  $p = 20$ ), was used for the SW measurements by varying the X-ray incidence angles  $\theta$  around the Bragg angle  $\theta_B$ . The photoemission yield distribution of (b) SW-HXPS ( $h\nu = 3000$  eV) and (c) SW-RXPS ( $h\nu = 459$  eV). (d) The RIXS yield distribution of SW-RIXS ( $h\nu = 459.3$  eV). The yield distribution demonstrates the probing depth sensitivity of these techniques. The probing depth for RXPS and HXPS ( $3\lambda$ ) is  $\sim 27$  and  $135$  Å, respectively, as indicated in b and c. The probing depth for RIXS ( $3\lambda$ ) is  $960$  Å (not indicated in d). According to the probing depths, SW-RXPS is sensitive to the top LAO layer and the first interface, SW-HXPS is sensitive to the top 3 LAO/STO (STO/LAO) interfaces, and SW-RIXS is sensitive to all 20 LAO/STO (STO/LAO) interfaces.



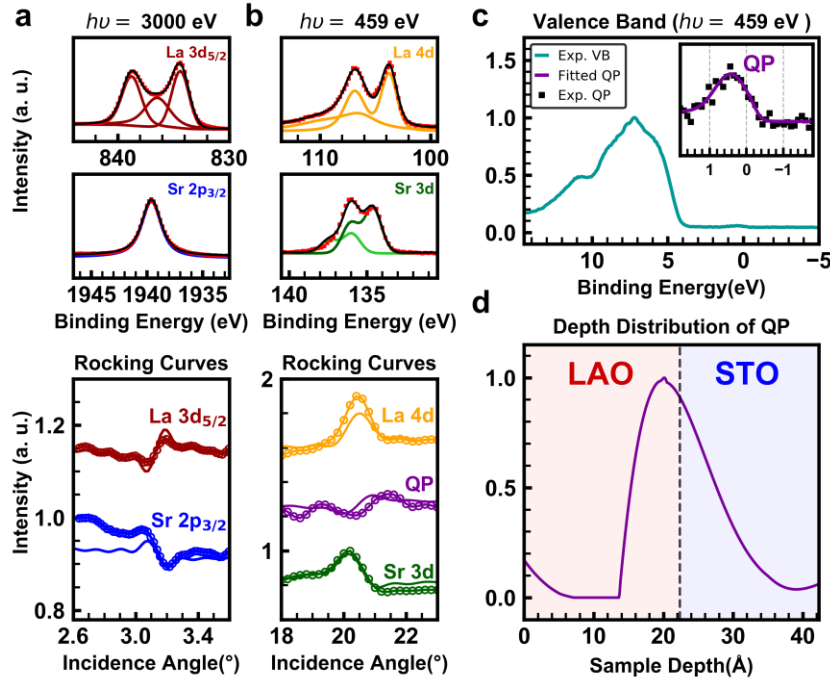


**Figure 2 | SW photoemission results and the depth distribution of the QP peak.** (a) SW-HXPS results ( $h\nu = 3000$  eV) (b)&(c)&(d) SW-RXPS results ( $h\nu = 459$  eV). (a) The top panel is the fitted core-level spectra of La  $3d_{5/2}$  and Sr  $2p_{3/2}$  at an off-Bragg angle. The bottom panel shows their experimental (open circle) and best-fit (curve) rocking curves. (b) The top panel is the fitted core-level spectra of La  $4d$  and Sr  $3d$ . The bottom panel shows the experimental and theoretical rocking curves. For the QP peak, its spectrum is shown in c. (c) A valence band spectrum with an inset of the fitted QP peak near the Fermi level. The QP peak is fitted using Voigt function and Fermi-Dirac distribution. (d) The determined depth profile of the QP peak in the top LAO/STO bilayer. The sample depth of zero means the sample surface.

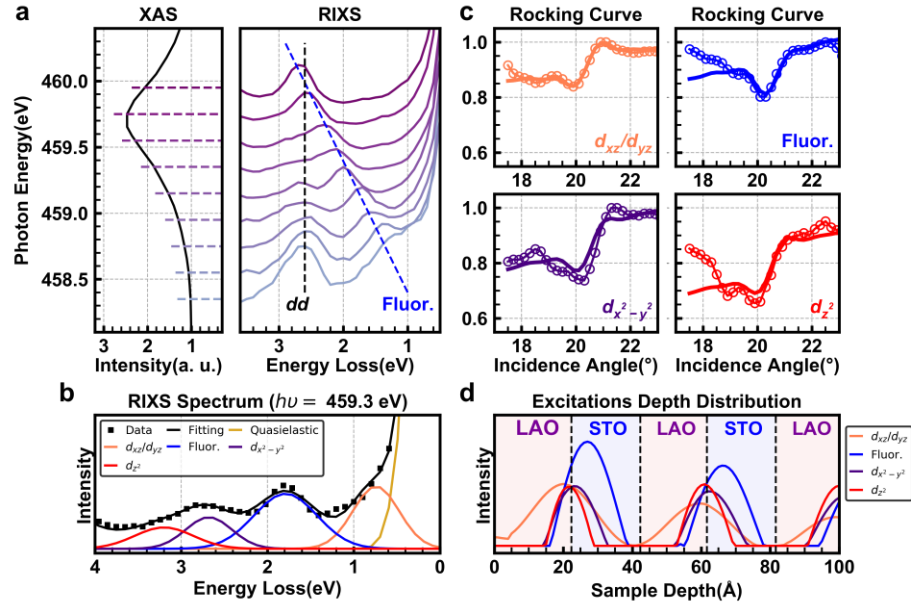


**Figure 3 | SW-RIXS result and depth distribution of  $dd$  excitations.** (a) The excitation-energy-dependent RIXS spectra were collected with excitation energies around the Ti  $L_3$  XAS edge, ranging from 459.7 to 458.1 eV and marked by colour dashed lines in the XAS panel. In the RIXS panel, the black and blue dashed lines are guides to the eyes to show the evolution of the Raman (black) and fluorescence (blue) spectral features, respectively. (b) RIXS spectrum collected using an excitation photon energy of 459.3 eV at an off-Bragg angle for the SW-RIXS measurements. The RIXS spectrum consists of a quasielastic,  $d_{xz}/d_{yz}$ ,  $d_{x^2-y^2}$ ,  $d_{z^2}$ , and fluorescence excitations. (c) Experimental (open circle) and best-fit (curve) rocking curves for  $d_{xz}/d_{yz}$ , fluorescence,  $d_{x^2-y^2}$ , and  $d_{z^2}$  excitations. The color scheme in this panel adopts that in panel (b). (d) Determined depth profiles of these RIXS excitations in the top 5 interfaces of LAO/STO heterostructures.

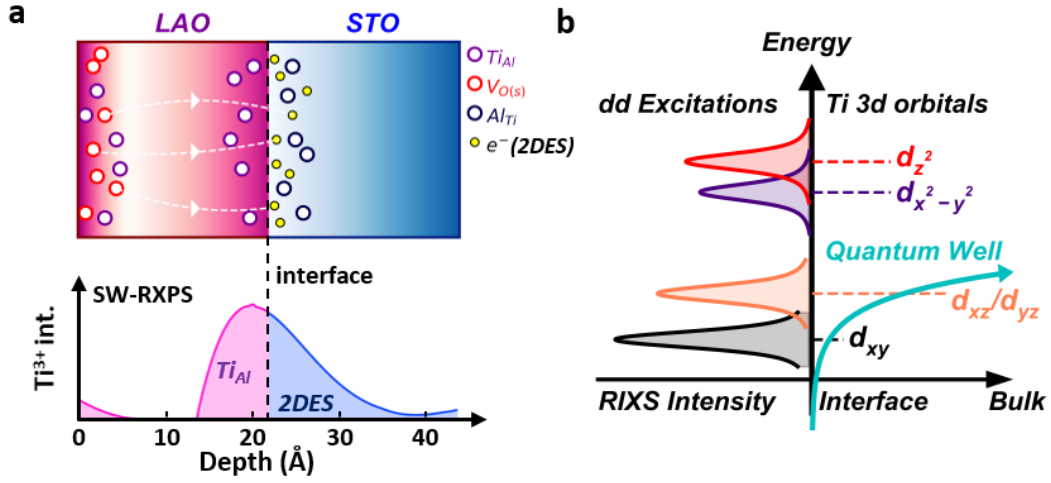


**Figure 4 | Formation and subband energy levels of a 2DES at a LAO/STO interface.**

(a) Illustration of the polarity-induced defect mechanism that leads to the 2DES formation. Paired antisite defects ( $\text{Ti}_{\text{Al}}$  in the LAO layer and  $\text{Al}_{\text{Ti}}$  in the STO layer) form in order to alleviate the polarisation-induced field across the LAO/STO interfaces. When the LAO layer is below the critical thickness (3 uc), all electrons transferred from  $\text{Ti}_{\text{Al}}$  in the LAO layer are trapped by the deep  $\text{Al}_{\text{Ti}}$  defects in the STO layer, causing no mobile electron. In contrast, with LAO layer thickness over 3 uc, the surface oxygen vacancy defects ( $\text{V}_{\text{O(s)}}$ ) start to donate half of the electrons to  $\text{Al}_{\text{Ti}}$  defects, and the rest to form the 2DES ( $\text{e}^-$ ) in the STO layer. The  $\text{Ti}_{\text{Al}}$  defects ( $\text{Ti}^{3+}$ ) can be probed by RXPS and RIXS. The lower panel is the SW-RXPS-determined depth profile, showing two main  $\text{Ti}^{3+}$  sources. One source in STO is 2DES in the STO and the other is  $\text{Ti}_{\text{Al}}$  in the LAO, matching the polarity-induced defect mechanism. (b) The orbital transitions from ground state ( $d_{xy}$ ) to final states ( $d_{xz}/d_{yz}$ ,  $d_{x^2-y^2}$ , and  $d_{z^2}$ ) are responsible for the  $dd$  RIXS process. The distributions of these  $dd$  excitations are affected by the quantum confinement effect.

## References

1. Ohtomo, A. & Hwang, H. A high mobility electron gas at the  $\text{LaAlO}_3/\text{SrTiO}_3$  heterointerface. *Nature* **427**, 423-426 (2004).
2. Huijben, M. et al. Electronically coupled complementary interfaces between perovskite band insulators, *Nat. Mater.* **5**, 556 (2006).
3. Thiel, S. et al. Tunable quasi-two-dimensional electron gases in oxide heterostructures. *Science* **313**, 1942-1945 (2006).
4. Brinkman, A. et al. Magnetic effects at the interface between non-magnetic oxides, *Nat. Mater.* **6**, 493-496 (2007).
5. Hwang, H. Y. et al. Emergent phenomena at oxide interfaces. *Nat. Mater.* **11**, 103-113 (2012).
6. Salluzzo, M. et al. Orbital reconstruction and the two-dimensional electron gas at the  $\text{LaAlO}_3/\text{SrTiO}_3$  interface. *Phys. Rev. Lett.* **102**, 166804 (2009).
7. Nakagawa, N., et al. Why some interfaces cannot be sharp. *Nat. Mater.* **5**, 204-209 (2006).
8. Herranz, G. et al. High mobility in  $\text{LaAlO}_3/\text{SrTiO}_3$  heterostructures: Origin, dimensionality, and perspectives. *Phys. Rev. Lett.* **98**, 216803 (2007).
9. Willmott, P. R. et al. Structural basis for the conducting interface between  $\text{LaAlO}_3$  and  $\text{SrTiO}_3$ . *Phys. Rev. Lett.* **99**, 155502 (2007).
10. Cen, C. et al. Nanoscale control of an interfacial metal-insulator transition at room temperature. *Nat. Mater.* **7**, 298-302 (2008).
11. Huijben, M. et al. Structure-property relation of  $\text{SrTiO}_3/\text{LaAlO}_3$  interfaces, *Adv. Mater.* **21**, 1665-1677 (2009).
12. Zhong, Z. C., et al. Polarity-induced oxygen vacancies at  $\text{LaAlO}_3/\text{SrTiO}_3$  interfaces. *Phys. Rev. B* **82**, 165127 (2010).
13. Pentcheva, R. et al. Parallel electron-hole bilayer conductivity from electronic interface reconstruction, *Phys. Rev. Lett.* **104**, 166804 (2010).
14. Qiao, L. et al. Cation mixing, band offsets and electric fields at  $\text{LaAlO}_3/\text{SrTiO}_3(001)$  heterojunctions with variable La:Al atom ratio. *Surf. Sci.* **605**, 1381-1387 (2011).
15. Salluzzo, M. et al. Structural and electronic reconstructions at the  $\text{LaAlO}_3/\text{SrTiO}_3$  interface, *Adv. Mater.* **25**, 2333-2338 (2013).
16. Fongkaew, I. et al. Effects of structural relaxation, and surface termination on two-dimensional electron gas formation at the  $\text{LaAlO}_3/\text{SrTiO}_3(001)$  interface. *Phys. Rev. B* **92**, 155416 (2015).
17. Yu, L. & Zunger, A. A polarity-induced defect mechanism for conductivity and magnetism at polar-nonpolar oxide interfaces. *Nat. Commun.* **5**, 5118 (2014).
18. Sing, M. et al. Profiling the interface electron gas of  $\text{LaAlO}_3/\text{SrTiO}_3$  heterostructures with hard x-ray photoelectron spectroscopy. *Phys. Rev. Lett.* **102**, 176805 (2009).
19. Santander-Syro, A. F. et al. Two-dimensional electron gas with universal subbands at the surface of  $\text{SrTiO}_3$ . *Nature* **469**, 189-193 (2011).
20. Cancellieri, C. et al. Polaronic metal state at the  $\text{LaAlO}_3/\text{SrTiO}_3$  interface. *Nat. Commun.* **7**, 10386 (2016).
21. Drera, G. et al. Spectroscopic evidence of in-gap states at the  $\text{SrTiO}_3/\text{LaAlO}_3$  ultrathin interfaces. *Appl. Phys. Lett.* **98**, 052907 (2011).

22. Koitzsch, A. et al. In-gap electronic structure of  $\text{LaAlO}_3\text{-SrTiO}_3$  heterointerfaces investigated by soft x-ray spectroscopy. *Phys. Rev. B* **84**, 245121 (2011).
23. Berner, G. et al. Direct k-space mapping of the electronic structure in an oxide-oxide interface. *Phys. Rev. Lett.* **110**, 247601 (2013).
24. Plumb, N. C., et al. Evolution of the  $\text{SrTiO}_3$  surface electronic states as a function of  $\text{LaAlO}_3$  overlayer thickness. *Appl. Surf. Sci.* **412**, 271-278 (2017).
25. Zhou, K.-J. et al. Localized and delocalized Ti 3d carriers in  $\text{LaAlO}_3/\text{SrTiO}_3$  superlattice revealed by resonant inelastic x-ray scattering. *Phys. Rev. B* **83**, 201402(R) (2011).
26. Pfaff, F. et al. Raman and fluorescence contributions to the resonant inelastic soft x-ray scattering on  $\text{LaAlO}_3/\text{SrTiO}_3$  heterostructures. *Phys. Rev. B* **97**, 035110 (2018).
27. Basletic, M. et al. Mapping the spatial distribution of charge carriers in  $\text{LaAlO}_3/\text{SrTiO}_3$  heterostructures. *Nat. Mater.* **7**, 621-625 (2008).
28. Huang, B.-C. et al. Mapping band alignment across complex oxide heterostructures. *Phys. Rev. Lett.* **109**, 246807 (2012).
29. Lee, P. W. et al. Hidden lattice instabilities as origin of the conductive interface between insulating  $\text{LaAlO}_3$  and  $\text{SrTiO}_3$ . *Nat. Commun.* **7**, 12773 (2016).
30. Song, K. et al. Direct imaging of the electron liquid at oxide interfaces. *Nat. Nano.* **13**, 198-203 (2018).
31. Gauquelin, N., Hawthorn, D. G., et al. Atomic scale real-space mapping of holes in  $\text{YBa}_2\text{Cu}_3\text{O}_{6+\delta}$ . *Nat. Commun.* **5**, 1 (2014).
32. Löffler, S. et al. Real-space mapping of electronic orbitals. *Ultramicroscopy* **177**, 26-29 (2017).
33. Egerton, R. F. Scattering delocalization and radiation damage in STEM-EELS. *Ultramicroscopy* **180**, 115-124 (2017).
34. Jeong, J. S. et al. Probing core-electron orbitals by scanning transmission electron microscopy and measuring the delocalization of core-level excitations. *Phys. Rev. B* **93**, 165140 (2016).
35. Gray, A.-X., Papp, C., Balke, B. et al. Interface properties of magnetic tunnel junction  $\text{La}_{0.7}\text{Sr}_{0.3}\text{MnO}_3/\text{SrTiO}_3$  superlattices studied by standing-wave excited photoemission spectroscopy. *Phys. Rev. B* **82**, 205116 (2010).
36. Kaiser, A. M. et al. Suppression of near-Fermi level electronic states at the interface in a  $\text{LaNiO}_3/\text{SrTiO}_3$  Superlattice, *Phys. Rev. Lett.* **107**, 116402 (2011).
37. Yang, S.-H. et al. Making use of x-ray optical effects in photoelectron-, Auger electron-, and x-ray emission spectroscopies: Total reflection, standing-wave excitation, and resonant effects, *J. Appl. Phys.* **113**, 073513 (2013).
38. Lin, S.-C. et al. Interface properties and built-in potential profile of a  $\text{LaCrO}_3/\text{SrTiO}_3$  superlattice determined by standing-wave excited photoemission spectroscopy. *Phys. Rev. B* **98**, 165124 (2018).
39. Conlon, C. S. et al. Hard x-ray standing-wave photoemission insights into the structure of an epitaxial  $\text{Fe/MgO}$  multilayer magnetic tunnel junction. *J. Appl. Phys.* **126**, 075305 (2019).
40. Kuo, C.-T., Lin, S.-C. et al. Depth-resolved resonant inelastic x-ray scattering at a superconductor/half-metallic-ferromagnet interface through standing wave excitation. *Phys. Rev. B* **98**, 235146 (2018).

- 
41. Huijben, M. et al. Defect engineering in oxide heterostructures by enhanced oxygen surface exchange, *Adv. Funct. Mater.* **23**, 5240-5248 (2013).
  42. Huijben, M. et al. Modified spin relaxation mechanism by tunable coupling between interfacial two-dimensional electron gases in correlated oxide heterostructures. *Phys. Rev. B* **96**, 075310 (2017).
  43. Huijben, M. et al. Enhanced local magnetization by interface engineering in perovskite-type correlated oxide heterostructures. *Adv. Mater. Interfaces* **2**, 1400416 (2015).
  44. Rueff, J.-P. et al. The GALAXIES beamline at the SOLEIL synchrotron: inelastic X-ray scattering and photoelectron spectroscopy in the hard X-ray range, *J. Synchrotron Rad.* **22**, 175 (2015).
  45. Chuang, Y.-D. et al. Momentum-resolved resonant inelastic soft X-ray scattering (qRIXS) endstation at the ALS, *J. Elec. Spec. Relat. Phemon.*, In Press (2019).

# Supplementary Information

## Two-dimensional electron systems in perovskite oxide heterostructures: Role of the polarity-induced substitutional defects

Shih-Chieh Lin,<sup>1,2</sup> Cheng-Tai Kuo,<sup>1,2,3,\*</sup> Yu-Cheng Shao,<sup>4</sup> Yi-De Chuang,<sup>4</sup> Jaap Geessinck,<sup>5</sup> Mark Huijben,<sup>5</sup> Jean-Pascal Rueff,<sup>6,7</sup> Ismael L. Graff,<sup>8</sup> Giuseppina Conti,<sup>1,2</sup> Yingying Peng,<sup>9,#</sup> Aaron Bostwick,<sup>4</sup> Eli Rotenberg,<sup>4</sup> Eric Gullikson,<sup>2</sup> Slavomír Nemšák,<sup>4</sup> Arturas Vailionis,<sup>10,11</sup> Nicolas Gauquelin,<sup>5,12</sup> Johan Verbeeck,<sup>12</sup> Giacomo Ghiringhelli,<sup>9</sup> Claus M. Schneider,<sup>1,13</sup> and Charles S. Fadley<sup>1,2,†</sup>

<sup>1</sup> Department of Physics, University of California Davis, Davis, California 95616, USA

<sup>2</sup> Materials Sciences Division, Lawrence Berkeley National Laboratory, Berkeley, California 94720, USA

<sup>3</sup> Stanford Synchrotron Radiation Lightsource, SLAC National Accelerator Laboratory, Menlo Park, California 94025, USA

<sup>4</sup> Advanced Light Source, Lawrence Berkeley National Laboratory, Berkeley, California 94720, USA

<sup>5</sup> Faculty of Science and Technology and MESA+ Institute for Nanotechnology, University of Twente, Enschede 7500 AE, The Netherlands

<sup>6</sup> Synchrotron SOLEIL, L'Orme des Merisiers, Saint-Aubin-BP48, 91192 Gif-sur-Yvette, France

<sup>7</sup> Sorbonne Université, CNRS, Laboratoire de Chimie Physique-Matière et Rayonnement, 75005 Paris, France

<sup>8</sup> Department of Physics, Federal University of Paraná, Curitiba, Brazil

<sup>9</sup> CNR-SPIN and Dipartimento di Fisica Politecnico di Milano, Piazza Leonardo da Vinci 32, Milano I-20133, Italy

<sup>10</sup> Stanford Nano Shared Facilities, Stanford University, Stanford, California 94305, USA

<sup>11</sup> Department of Physics, Kaunas University of Technology, Studentu street 50, LT-51368 Kaunas, Lithuania

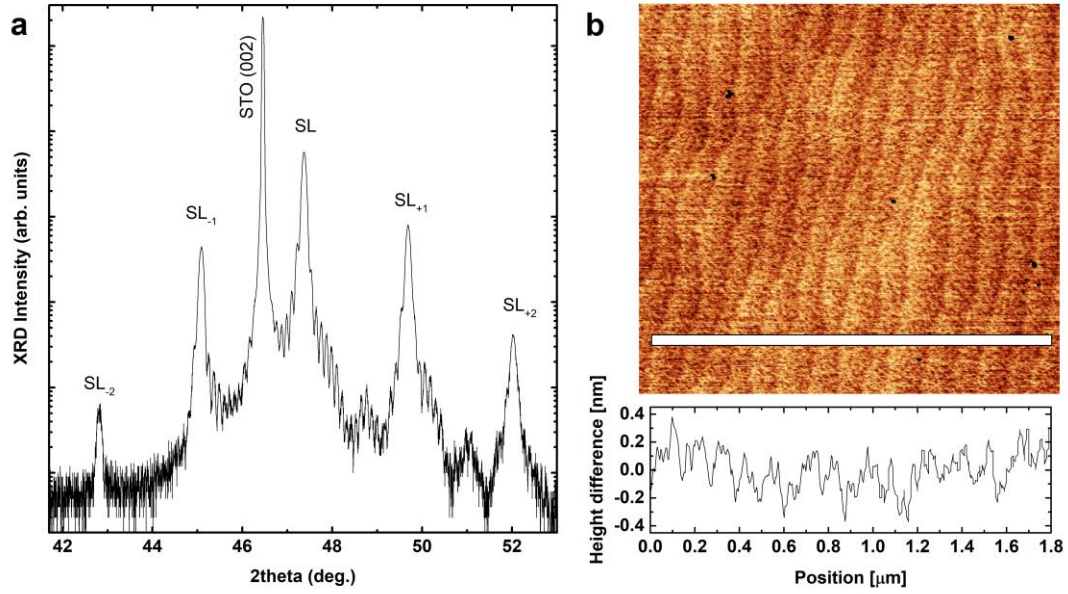
<sup>12</sup> Electron Microscopy for Materials Science (EMAT), University of Antwerp, Groenenborgerlaan 171, B-2020 Antwerp, Belgium

<sup>13</sup> Peter-Grünberg-Institut PGI-6, Forschungszentrum Jülich, Jülich 52425, Germany

\* Email: ctkuo@slac.stanford.edu

# Present address: International Center for Quantum Materials, School of Physics, Peking University, Beijing 100871, China

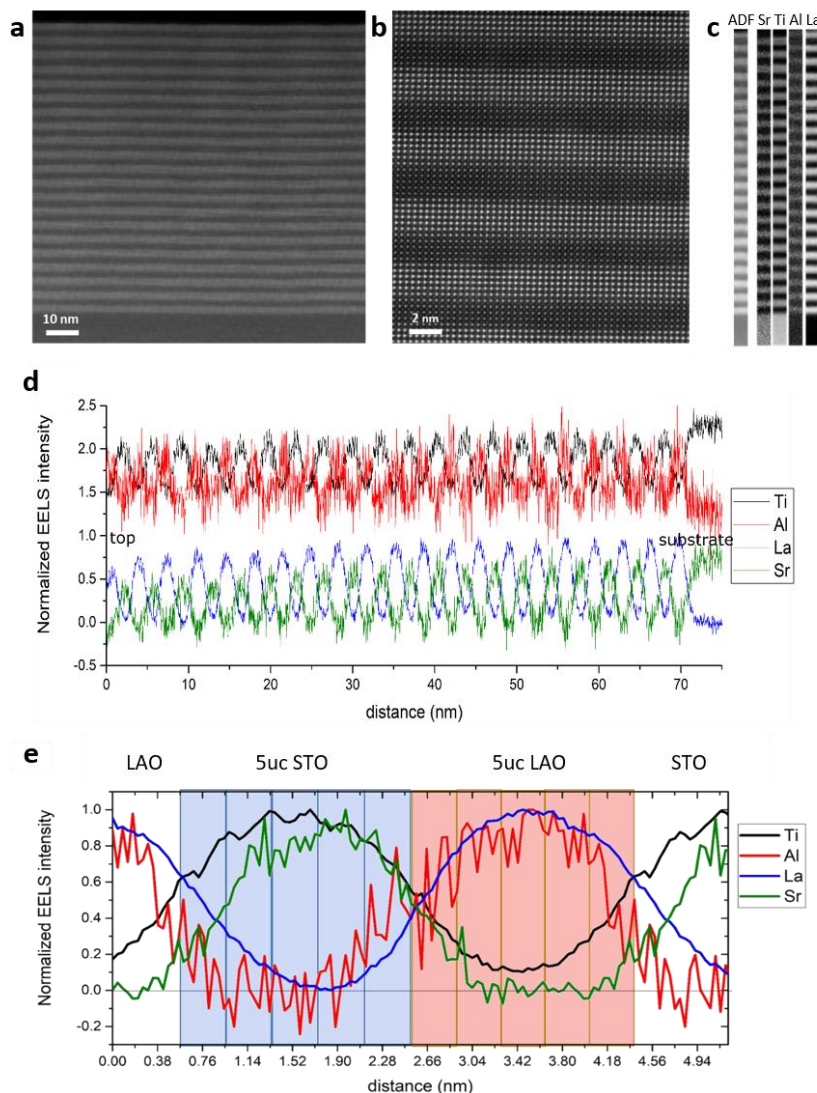
† Deceased August 1, 2019.



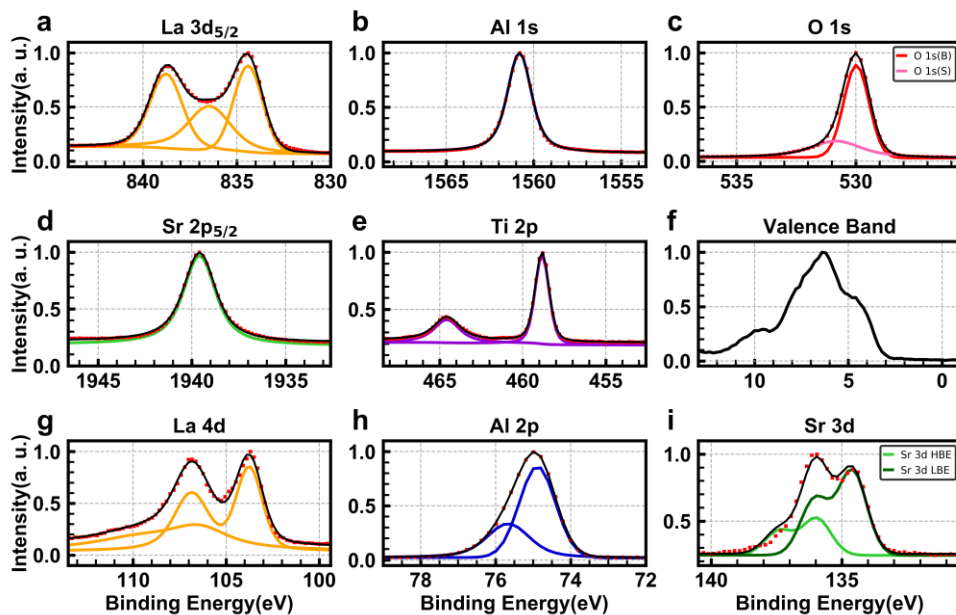
**Supplementary Figure 1 | Structural characterisation of the LAO/STO superlattice.**

(a) X-ray diffraction analysis of the out-of-plane crystalline ordering of the LAO/STO superlattice. The XRD results showed a reduced c-axis parameter of 3.73 Å for each LAO layer as compared to 3.90 Å for each STO layer, (b) Atomic force microscopy image (1.9  $\mu m$  x 1.9  $\mu m$ ) of the superlattice surface. The topology and averaged line profile (white rectangle) show smooth terraces separated by clear, single-unit-cell height steps similar to the surface of the initial  $TiO_2$ -terminated STO (001) substrate.

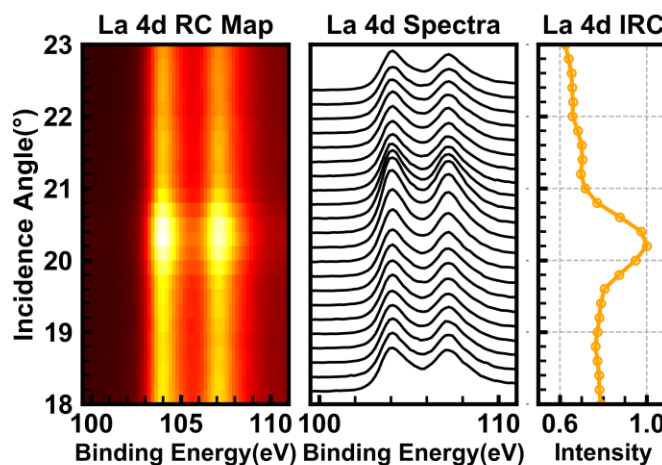




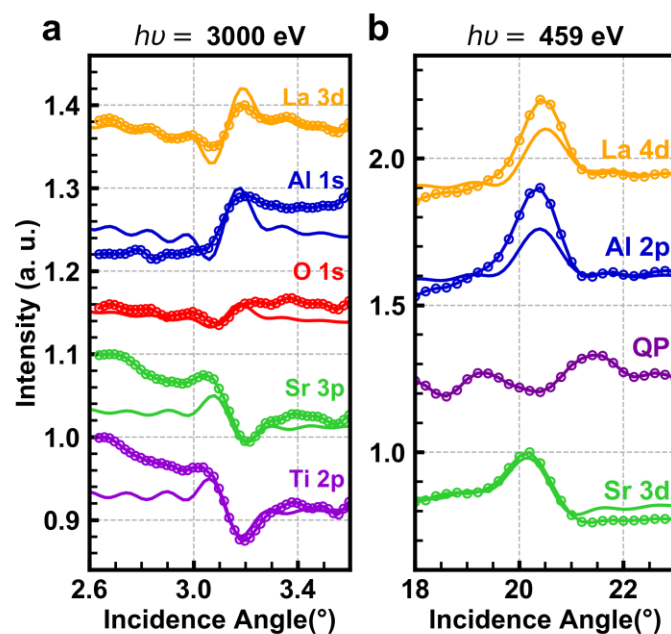
**Supplementary Figure 2 | STEM characterisation of the LAO/STO superlattice.** (a) HAADF overview image of the all sample of 20 repetitions of LAO(5uc)/STO(5uc) on STO substrate showing the great growth control of the specimen. (b) HAADF high magnification image of a region of 5,5 periods showing the presence of local roughness of  $\pm 1$  uc at each interface. (c) EELS two-dimensional elemental maps of the Sr  $L_{2,3}$ , Ti  $L_{2,3}$ , Al K, and La  $M_{4,5}$  edges with the corresponding ADF signal simultaneously acquired showing the great compositional control over each interfaces of the superlattice. (d) EELS line profile of the Ti  $L_{2,3}$ , Sr  $L_{2,3}$ , Al K and La  $M_{4,5}$  edges showing the limited interdiffusion on both the A (Sr/La) and the B (Ti/Al) sites of the perovskite. (e) Average compositional profile over a region of 1,5 period of the superlattice showing the dissymmetry of the interfaces in terms of interdiffusion on the A site.



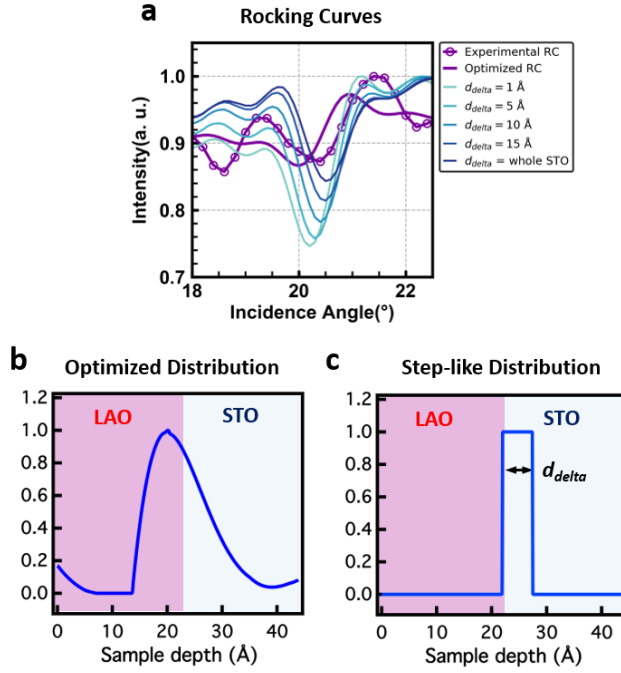
**Supplementary Figure 3 | Core-level and valence band spectra collected by HXPS and RXPS.** Core level and valence band spectra measured at an off-Bragg angle for (a)-(f) SW-HXPS and (g)-(i) SW-RXPS measurements. The core level spectra were fitted using Voigt function and Shirley background.



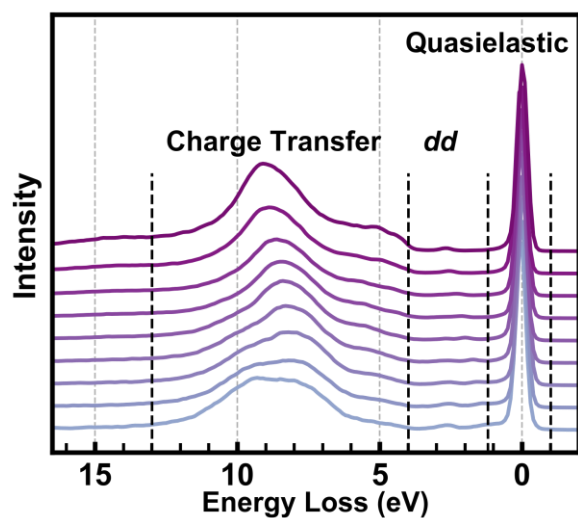
**Supplementary Figure 4 | Demonstration of deriving an experimental RC.** The left panel is the RC map of La 4d and the middle panel is the corresponding plots of La 4d spectra. Simply plot the integrated core-level peak intensities versus the incidence angles (integrated RC, IRC) can already show the intensity modulation of ~25%, a direct indication of SW effect. For the RCs in Fig. 2 and supplementary Fig. 4, The Shirley background contributions were removed for more careful investigations of the SW effect.



**Supplementary Figure 5 | Core-level and QP rocking curves collected by SW-HXPS and SW-RXPS. (a) Core-level rocking curves collected by SW-HXPS. (b) Core-level and QP rocking curves collected by SW-RXPS.**



**Supplementary Figure 6 | Comparison of the QP expt. RC with simulations using various QP depth distribution.** (a) The QP expt. RC (also in Fig. 2(b)) and simulated RCs using optimised and step-like distributions. The optimised distribution is demonstrated in (b) and the step-like distributions is in (c). The best-fit RC shown in Fig. 2(b) was simulated using the optimised distribution. For the step-like distribution, when  $d_{\text{delta}} = \text{whole STO}$ , it means that it is the case of uniform distribution in the whole STO layer. The errors of different distributions are summarized in supplementary Table 1.



**Supplementary Figure 7 | Excitation-energy-dependent RIXS spectra with wide energy loss range.** These RIXS spectra were collected with identical excitation energy range and show the energy loss region of -2~16.5 eV. The quasielastic, *dd*, and charge transfer peaks are separated by the dashed lines.

**Supplementary Table 1 | Summary of mean square errors assuming different depth distribution**

<b>Distribution</b>	<b>Mean square errors</b>
<b>Optimised</b>	$9.1 \times 10^{-4}$
<b>Step-like, <math>d_{\text{delta}} = 1 \text{ \AA}</math></b>	$3.1 \times 10^{-3}$
<b>Step-like, <math>d_{\text{delta}} = 5 \text{ \AA}</math></b>	$2.8 \times 10^{-3}$
<b>Step-like, <math>d_{\text{delta}} = 10 \text{ \AA}</math></b>	$2.8 \times 10^{-3}$
<b>Step-like, <math>d_{\text{delta}} = 15 \text{ \AA}</math></b>	$2.9 \times 10^{-3}$
<b>Step-like, <math>d_{\text{delta}} = \text{whole STO}</math></b>	$2.9 \times 10^{-3}$

## Supplementary Note 1

### Characterisation of the LAO/STO superlattice

The superlattice sample,  $[(\text{LAO})_5/(\text{STO})_5]_{20}$ , was characterized to confirm exhibiting flat surface and high crystallinity. X-ray diffraction (XRD) data in Supplementary Fig. 1a show clear Laue fringes between the diffraction peaks. The atomic force microscopy image in Supplementary Fig. 1b shows smooth step terraces, similar to the surface of the initial  $\text{TiO}_2$ -terminated STO (001) substrate. Supplementary Fig. 2 shows the results of STEM characterisation. On the one hand at the STO\_bottom/LAO\_top interface which can be assimilated to a "SrO/ $\text{AlO}_2$ /LaO" interface, Sr and Ti diffuse 1-1.5uc inside the LAO, and La and Al diffuse 1-1.5uc inside the STO, this results in the following stacking:  $\text{TiO}_2$ -SrO- $\text{Ti}_{0.6}\text{Al}_{0.4}\text{O}_2$ - $\text{La}_{0.5}\text{Sr}_{0.5}\text{O}$ - $\text{Ti}_{0.4}\text{Al}_{0.6}\text{O}_2$ - $\text{La}_{0.9}\text{Sr}_{0.1}\text{O}$ - $\text{Ti}_{0.1}\text{Al}_{0.9}\text{O}_2$ -LaO. On the other hand, at the LAO\_bottom/STO\_top interface which can be assimilated to a "LaO/ $\text{TiO}_2$ /SrO" interface, Sr diffuse 1uc inside the LAO whereas Ti diffuses over 2uc, and Al diffuses 1uc inside the STO whereas La diffuses over 3 uc, this results in the following stacking:  $\text{AlO}_2$ -LaO- $\text{Ti}_{0.2}\text{Al}_{0.8}\text{O}_2$ - $\text{La}_{0.9}\text{Sr}_{0.1}\text{O}$ - $\text{Ti}_{0.7}\text{Al}_{0.3}\text{O}_2$ - $\text{La}_{0.5}\text{Sr}_{0.5}\text{O}$ - $\text{TiO}_2$ - $\text{La}_{0.2}\text{Sr}_{0.8}\text{O}$ - $\text{TiO}_2$ - $\text{La}_{0.1}\text{Sr}_{0.9}\text{O}$ . Note that a diffusion of 1uc can be attributed to roughness and the accuracy of concentrations can be overestimated to 0.1. We can therefore conclude that the STO\_bottom/LAO\_top interface is sharper whereas the LAO\_bottom/STO\_top interface is more diffused. This confirms observation made by other authors<sup>7,43</sup> and theoretical predictions<sup>16</sup>. The presence of around 10% of Ti at the center of the LAO indicating a larger diffusion length of Ti inside the LAO (of the order of 2.5-3uc) cannot be excluded, but can be mitigated by the presence of electron delocalisation/channelling over 4-5 Angstrom(1uc) beyond the scope of this paper.

## Supplementary Note 2

### Fitting of core-level rocking curves

A core-level rocking curve (RC) is defined as the fitted core-level peak intensities versus incidence angles. Supplementary Fig. 3 shows the strongest core-level spectra for all atomic species in the LAO/STO superlattice at an off-Bragg angle. The core levels were fitted using Shirley background and Voigt function. The demonstration of observing an SW effect in the raw data is shown in Supplementary Fig. 4. The left panel in



Supplementary Fig. 4 is the La 4d RC map and the middle panel shows the corresponding core-level spectra at a series of incidence angles. By simply integrating the peak intensity along the binding energy axis at each incidence angle (so called IRC), one can observe clear intensity modulation of 25%, as shown in the right panel of Supplementary Fig. 4. To have more careful investigation of SW effects, we use the fitted core-level peak intensities (so called RC) for all the analyses in this work. The experimental and best-fit RCs are demonstrated in Supplementary Fig. 5.

### **Supplementary Note 3**

#### **Comparison of simulated RCs using various depth distribution**

We use the QP RC as an example to show that the difference between the experimental and simulated RCs using the optimised (best-fit), step-like ( $d_{\text{delta}}=1\sim15\text{ \AA}$ ), and uniform ( $d_{\text{delta}}=\text{whole STO layer}$ ), distributions. Supplementary Fig. 5a shows the QP experimental RC along with simulated RCs using various depth distribution. Simply inspect by eyes, the simulated RC using optimised distribution is close to the experimental data the most. Supplementary Fig. 6b&c shows the optimised distribution and step-like distribution. The step-like distribution means that we assume the weighted factor (or concentration) equals one when  $d = 0$  to  $d_{\text{delta}}$  in the STO layer and the weighted factor equals zero elsewhere. In our analyses, the determined distributions for the best-fit results depend on the mean square errors. Supplementary table 1 summarizes the mean square errors of various distribution for the QP RC. It shows that the optimised distribution has the minimum errors ( $9.1\times10^{-4}$ ) while other distributions have roughly errors of  $\sim3\times10^{-3}$ . Therefore, the optimised distribution should be close to the reality the most.

### **Supplementary Note 4**

#### **Wide-energy-loss-range RIXS spectra**

Supplementary Fig. 7 shows the excitation-energy-dependent RIXS spectra with energy loss region (-2~16.5 eV).